

CO₂ Reduction Hot PaperHow to cite: *Angew. Chem. Int. Ed.* **2021**, *60*, 24838–24843

International Edition: doi.org/10.1002/anie.202109600

German Edition: doi.org/10.1002/ange.202109600

Facet-Selective Deposition of Ultrathin Al₂O₃ on Copper Nanocrystals for Highly Stable CO₂ Electroreduction to Ethylene

Hui Li⁺, Peiping Yu⁺, Renbo Lei⁺, Feipeng Yang, Peng Wen, Xiao Ma, Guosong Zeng, Jinghua Guo, Francesca M. Toma, Yejun Qiu, Scott M. Geyer, Xinwei Wang, Tao Cheng,* and Walter S. Drisdell*

Abstract: Catalysts based on Cu nanocrystals (NCs) for electrochemical CO₂-to-C₂₊ conversion with high activity have been a subject of considerable interest, but poor stability and low selectivity for a single C₂₊ product remain obstacles for realizing sustainable carbon-neutral cycles. Here, we used the facet-selective atomic layer deposition (FS-ALD) technique to selectively cover the (111) surface of Cu NCs with ultrathin Al₂O₃ to increase the exposed facet ratio of (100)/(111), resulting in a faradaic efficiency ratio of C₂H₄/CH₄ for overcoated Cu NCs 22 times higher than that for pure Cu NCs. Peak performance of the overcoated catalyst (Cu NCs/Al₂O₃-10C) reaches a C₂H₄ faradaic efficiency of 60.4% at a current density of 300 mA cm⁻² in 5 M KOH electrolyte, when using a gas diffusion electrode flow cell. Moreover, the Al₂O₃ overcoating effectively suppresses the dynamic mobility and the aggregation of Cu NCs, which explains the negligible activity loss and selectivity degradations of Cu NCs/Al₂O₃-10C shown in stability tests.

Introduction

Developing highly efficient electrocatalysts for converting CO₂ into value-added chemical fuels provides a feasible pathway for renewable energy storage while reducing the depletion of fossil resources.^[1] Colloidal copper-based nanocrystals (Cu NCs) with various sizes, shapes, exposed facets, oxidation states, and surface ligands have been widely studied as electrocatalysts that can form multiple hydrocarbon products. However, the efficiency and selectivity are still too low for industrial-scale implementation.^[2,3] Hori and Takahashi et al. have demonstrated that the Cu (100) facet facilitates the formation of ethylene while the Cu (111) facet favors methane generation.^[4,5] This model catalyst study has inspired

the exploration of colloidal Cu NCs with dominantly exposed (100) facets for enhancing CO₂-to-C₂H₄ selectivity.^[6,7] However, these shape-controlled nanocrystals underwent unpredictable surface reconstructions and size changes during catalysis, which led to the loss of the initially well-defined facets and a decrease of favorable active sites.^[8–10] Although particle confinement and surface ligand engineering strategies have been developed to mitigate the degradation of electrocatalytic activity on metal nanoparticles,^[11,12] more effective surface modification tools are demanded to stabilize the Cu NCs for high yield CO₂-to-C₂H₄ conversion under high current density.

Atomic layer deposition (ALD), a gas phase ultrathin film deposition technique based on self-limiting reactions, has been widely utilized to fabricate inert oxide overcoating with precise thicknesses on metal nanoparticle catalysts to prevent their coalescence under harsh reaction conditions.^[13,14] A thermal post-treatment process is generally adopted to convert the continuous overcoating into porous channels to promote reactant diffusion and accessibility of active surface sites, which will alter the surface morphologies and structures of underlying nanoparticles at high temperature.^[15,16] Area-selective ALD (AS-ALD) has been shown to selectively deposit an ultrathin oxide layer onto the desired sites of nanoparticle catalysts. Still, the surface-functionalized organic molecules for area blocking must be removed to enhance the intimate contact at the interface.^[17,18] By contrast, facet-selective ALD (FS-ALD) provides a more straightforward way to passivate or activate the desired sites via the intrinsic differences in binding energies of metal precursor on various facets of metal nanoparticle catalysts.^[19,20] Lu et al. demonstrated that the trimethylaluminum

[*] Dr. H. Li,^[+] Dr. G. Zeng, Dr. F. M. Toma, Dr. W. S. Drisdell

Joint Center for Artificial Photosynthesis, Chemical Sciences Division, Lawrence Berkeley National Laboratory
1 Cyclotron Road, Berkeley, California 94720 (USA)
E-mail: wsdrisdell@lbl.gov

P. Yu,^[+] Prof. Dr. T. Cheng
Institute of Functional Nano and Soft Materials, Soochow University
Suzhou 215123 (China)
E-mail: tcheng@suda.edu.cn

R. Lei,^[+] Prof. Dr. X. Wang
School of Advanced Materials, Shenzhen Graduate School, Peking University
Shenzhen 518055 (China)

Dr. F. Yang, Dr. J. Guo
Advanced Light Source, Lawrence Berkeley National Laboratory
1 Cyclotron Road, Berkeley, California 94720 (USA)

P. Wen, Prof. Dr. Y. Qiu

Shenzhen Engineering Lab of Flexible Transparent Conductive Films, Department of Materials Science and Engineering, Harbin Institute of Technology
Shenzhen 518055 (China)

X. Ma, Prof. Dr. S. M. Geyer
Department of Chemistry, Wake Forest University
Winston-Salem, North Carolina 27109 (USA)

[*] These authors contributed equally to this work.

Supporting information and the ORCID identification number(s) for the author(s) of this article can be found under:
 https://doi.org/10.1002/anie.202109600.

(TMA) precursors have facet-selective adsorption behavior on Pt and Pd during thermal ALD of Al_2O_3 layers, and the adsorption and dissociation of TMA on Cu (111) and Cu (100) are endothermic.^[21] Therefore, a surface chemistry engineering approach is a promising means of preferentially depositing an inert Al_2O_3 layer on Cu (111) facets while leaving Cu (100) facets intact, potentially enhancing CO_2 -to- C_2H_4 selectivity and long-term stability.

In this work, we developed an “ H_2O -TMA- H_2O -TMA” pulse sequence to replace the typical “TMA- H_2O -TMA- H_2O ” cycles to deposit ultrathin Al_2O_3 layer on supported Cu NCs (Figure 1a). The first H_2O pulse generates surface

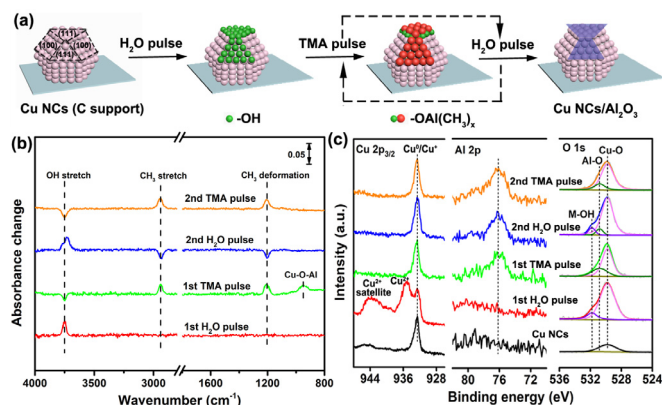


Figure 1. a) Schematic diagram of Al_2O_3 overcoated Cu nanocrystals generated with facet-selective ALD. b) In-situ infrared difference spectra and c) quasi in situ XPS of precursor dose cycles of the ALD process.

hydroxide groups on the Cu (111) facets, providing preferential nucleation sites for subsequent TMA adsorption and reaction. The Cu (100)/Cu (111) facet ratio for the optimized overcoated Cu NCs (10 cycles of ALD Al_2O_3 , Cu NCs/ Al_2O_3 -10C) is 7.5 times that of Cu NCs, which leads to a 22 fold increase in the faradaic efficiency ratio of $\text{C}_2\text{H}_4/\text{CH}_4$ in H-cell measurements. The overpotential for CO_2 -to- C_2H_4 is also decreased, attributed to a lower reaction energy barrier for the critical step of hydrogenation of $^*\text{CO}$ -CO to $^*\text{CO}$ -COH. Cu NCs/ Al_2O_3 -10C achieves a stable 60.4% Faradaic efficiency for C_2H_4 at a current density of 300 mA cm^{-2} in a polytetrafluoroethylene (PTFE)-based gas-diffusion electrode flow cell.

Results and Discussion

The Cu NCs were synthesized by following a previously reported method, with slight modifications (see the Experimental Methods in Supporting Information).^[22] The as-synthesized Cu NCs with pure cubic phase show a highly uniform spherical morphology with an average size of $10.0 \pm 1.6 \text{ nm}$ (Figure S1). The Cu NCs were well dispersed on carbon black with clear lattice fringes of (111) facets (Figure S2a–d). After 10 cycles of ALD Al_2O_3 , the Cu NCs were partially enclosed with an amorphous Al_2O_3 layer with $0.8 \pm 0.2 \text{ nm}$ thickness (Figure S2e–h). The overcoating thickness gradually increases with increasing ALD cycles of Al_2O_3

(Figure S3). In-situ infrared spectroscopy was carried out to gain insight into the surface reactions on Cu NCs during the thermal ALD process. As shown in Figure 1b, infrared difference spectra of pulsed precursors were used to illustrate the formation and elimination of surface groups by observing signal gain and loss, respectively. Spectral signatures of surface hydroxyl groups were observed at around 3752 cm^{-1} after the first H_2O pulse. They then disappeared after the subsequent TMA pulse, while signatures of surface CH_3 groups appeared/disappeared at around 2945 and 1204 cm^{-1} under TMA/ H_2O pulses.^[23] This alternating formation-consumption of surface groups is consistent with the self-limiting nature of typical ALD processes. A peak appeared at 953 cm^{-1} when delivering TMA precursors. It remained constant for the following cycles, indicating that the surface hydroxyl groups on Cu NCs were completely consumed by the first cycle of TMA, forming Cu-O-Al groups.^[24] During the second cycle H_2O pulse, the hydroxyl peak splits into a minor peak at 3770 cm^{-1} and a major peak of 3731 cm^{-1} , suggesting the presence of two chemically distinct hydroxyl groups as the active sites for the ALD reaction process evolved from Cu-OH to Al-OH groups.^[24] Quasi in situ X-ray photoelectron spectroscopy (XPS) was used to further investigate the surface chemistry of ALD doses,^[25] and the high resolution spectra of Cu 2p_{3/2}, Al 2p, and O 1s are shown in Figure 1c. Prior to ALD, the surface of the Cu NCs is composed of dominant metallic Cu and minor copper oxide species.^[26] The first dose of H_2O generated a large amount of CuO species, as indicated by the appearance of a sharp peak at 935.2 eV and a satellite peak at 943.9 eV .^[27] Moreover, surface hydroxyl groups with peaks at 531.8 eV are observed from O 1s spectra during the first and second H_2O pulses, consistent with the above in situ IR results. Interestingly, all detectable CuO disappeared during the following TMA pulse due to the strong reduction capacity of TMA precursors. It should be noted that the peaks of metallic copper (Cu^0) and copper (I) oxide are highly overlapped, and cannot rule out a certain amount of Cu_2O species on the surface. A peak at 530.8 eV from Al_2O_3 is also observed, and a shift in the intensity of peaks at 531.8 eV to 530.8 eV , indicates the transition of Cu-OH to Al-O.

Diffuse reflectance infrared Fourier transform spectroscopy (DRIFTS) of CO chemisorption has been widely used to determine the exposed facet distribution on metal catalysts.^[19–21] To confirm the facet-selective deposition mechanism of Al_2O_3 on Cu NCs, this technique was carried out on Cu NCs and Cu NCs/ Al_2O_3 -x (x = 5, 10, 20, 50) (Figure 2a and Figure S4). The three fitting peaks for the linear adsorption curves are assigned to CO adsorbed on the Cu (111) facet, Cu (100) facet, and low coordination Cu sites such as edges and corners (herein represented by Cu (211) facet), which matches well with the vibrational frequency peaks of calculated CO chemisorption (Figure S5 and Table S2). For the Cu NCs, the percentage of Cu (111) facet, Cu (100) facet, and Cu (211) over the surface is 48.2%, 40.6%, and 11.2%, respectively. After 5 ALD cycles of Al_2O_3 deposited on Cu NCs, the percentage of Cu (111) decreases from 48.2% to 36.0%, indicating that the Cu (111) surface sites are preferentially covered. The percentage of Cu (111) further

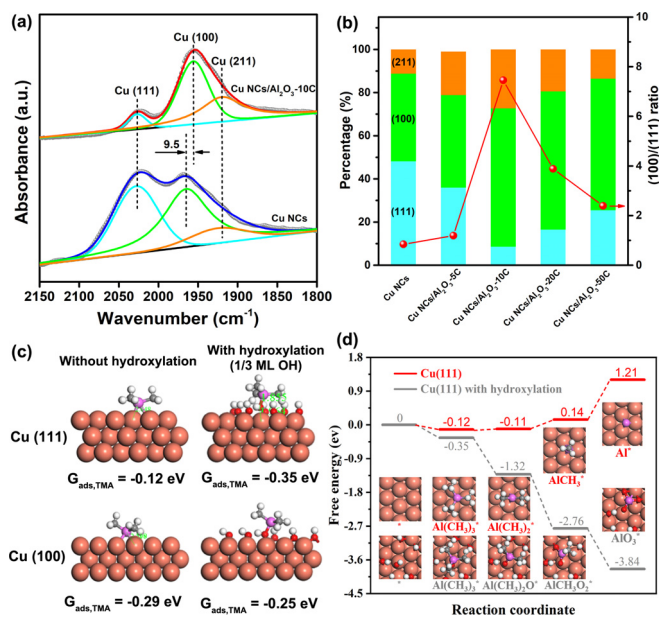


Figure 2. a) Fitted curves of DRIFTS CO linear adsorption peaks for Cu NCs and Cu NCs/Al₂O₃-10C catalysts. b) Facet percentage and (100)/(111) ratio of Cu NCs with different Al₂O₃ cycles. c) Free energies of a TMA precursor adsorbed on Cu surfaces with/without hydroxylation. d) Free energy profile (at 200 °C and 1 atm) for TMA dissociation on Cu (111) before and after hydroxylation.

decreases to 8.6% after 10 ALD cycles. However, excess ALD cycles start to cover Cu (100) facets, as indicated by a decrease in the integrated CO chemisorption peak area for Cu (100).

This facet-selective deposition process can be explained by the adsorption energy of TMA on different Cu facets, obtained from density functional theory (DFT) calculations. Figure 2c shows the calculated adsorption energies of TMA on Cu surfaces with or without hydroxylation. For the Cu surface without hydroxylation, the TMA molecule preferentially adsorbs on Cu (100) rather than Cu (111) indicated by the more negative adsorption energy. With hydroxylation, the trend reverses, with (111) binding TMA more strongly (−0.35 eV) than (100) does (−0.25 eV). Thus, the DFT calculations predict the preferential adsorption of TMA on Cu (111) after the H₂O pulse that provides abundant surface *OH. The DFT calculations also predict that surface *OH promotes the dissociation of TMA. The free energy profile in Figure 2d indicates that the TMA dissociation to Al* via Al(CH₃)₂* and AlCH₃* is exothermic with *OH at 200 °C. Such a process is not possible in pure Cu(111) (Figure 2d) or Cu (100) (Figure S6). Thus, the DFT calculations predict that TMA can decompose into Al₂O₃ that coated on Cu (111) surface, which well explains the experimental observations.

The CO₂ reduction reaction (CO₂RR) performance of Cu NCs with various ALD cycles was firstly evaluated in a three-electrode H-cell containing CO₂-saturated 0.5 M KHCO₃ as the flowing electrolyte. The geometric current density gradually decreased with increasing ALD cycles, as surface sites were blocked by the inert Al₂O₃ overcoating (Figure S7). Figure 3a shows the Faradaic efficiency (FE) of gas and liquid products over Cu NCs with various ALD cycles at a constant

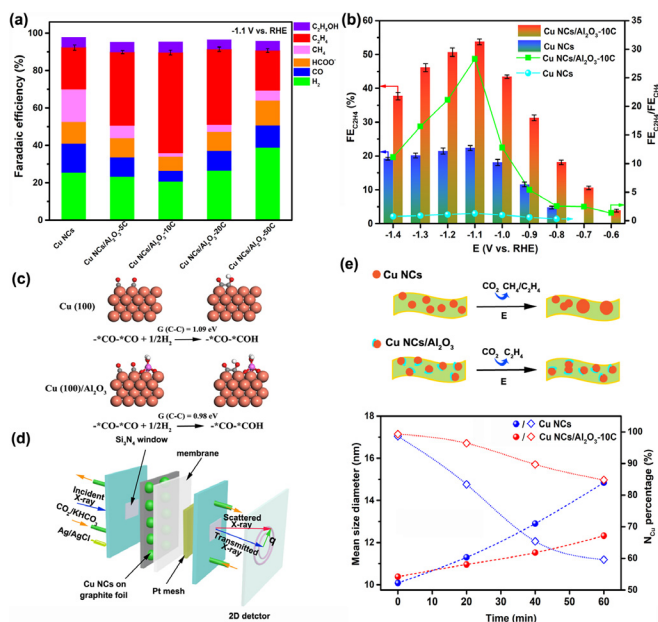


Figure 3. a) Faradaic efficiency (FE) of CO₂RR products for Cu NCs with different ALD cycles of Al₂O₃ overcoating at a constant potential of −1.1 V vs. RHE. The error bars indicate the standard deviation of three independent measurements. b) FE_{C₂H₄} and FE_{C₂H₄}/FE_{CH₄} ratio versus the potential for Cu NCs and Cu NCs/Al₂O₃-10C. c) The calculated free energy differences of hydrogenation of dimerized *CO*CO on Cu (100) and Cu (100)/Al₂O₃ from DFT calculation. d) Schematic diagram of an electrochemical flow cell for in situ small angle X-ray scattering (SAXS) characterization. e) Time-dependent mean size diameter and number density of nanocrystals from in situ SAXS, relative to the initial values at −1.1 V vs. RHE.

potential of −1.1 V vs. RHE. The FE of ethylene (FE_{C₂H₄}) for pure Cu NCs is only 22.4% due to the competing CH₄ formation and the sluggish C–C coupling steps.^[28] After 5 ALD cycles of Al₂O₃, a 1.75 times increase in FE_{C₂H₄} and a 2.6 times decrease in FE_{CH₄} were observed. As the Al₂O₃ overcoating increases to 10 cycles, the FE_{C₂H₄} increases to an impressive value of 53.8%, while FE_{CH₄} is reduced to 1.9%. By contrast, Cu NCs overcoated with 10 cycles Al₂O₃ by using reverse precursor pulse sequences (TMA-H₂O-TMA-H₂O, denoted as Cu NCs/Al₂O₃-10C-R) shows a much lower FE_{C₂H₄} of 15.9%, consistent with preferential deposition of Al₂O₃ on Cu (100) facets rather than Cu (111) facets (Figure S8). When the H₂O-TMA-H₂O-TMA ALD pulse cycles further increased to 20 and 50, the corresponding FE_{C₂H₄} decreases to 40.3% and 21.2%, respectively, and hydrogen becomes the dominant reaction product. Cu NCs/Al₂O₃-10C exhibits a 2.4-fold increase in FE_{C₂H₄} compared to the pure Cu NCs, consistent with the significant increase of (100)/(111) ratio on the NC surface. The trend of FE_{C₂H₄}/FE_{CH₄} at various ALD cycles is consistent with their partial current density ratio at −1.1 V vs. RHE (Figure S9). The onset potential for C₂H₄ generation over Cu NCs/Al₂O₃-10C is −0.6 V vs. RHE, which is more positive than that over Cu NCs. Such C₂ promotion is confirmed by DFT calculations showing a decrease of reaction energy of the potential-determining step (*CO*COH formation) from 1.09 eV to 0.98 eV (Figure 3c) on the Cu (100) surface. This large drop

implies that the heterointerface of Cu/Al₂O₃ does indeed help with steering selectivity towards C₂₊ products. Considering the inert nature of the Al₂O₃ overcoating and negligible effects on the electronic structure of Cu NCs (Figure S7b and Figure S10), the heterogeneous interface of Cu/Al₂O₃ mainly affects the adsorption orientation of neighbor *CO intermediates and therefore decreases the reaction energy of the potential-determining C–C coupling step. As the potential became more negative, both the FE_{C₂H₄} and FE_{C₂H₄}/FE_{CH₄} ratio reaches the maximum values of 53.8% and 28.3 at –1.1 V vs. RHE, respectively (Figure 3b). The electrochemically active surface area (ECSA) is estimated by measuring the electrical double-layer capacitance (Figure S11). The ECSA for Cu NCs/Al₂O₃-10C and Cu NCs is 17.5 and 36 cm², respectively, and the ratio of ECSA-normalized partial current density for C₂H₄ across the potential window is higher than 4.5 (Figure S12). Moreover, an enhancement of reaction kinetics for selective CO₂-to-C₂H₄ conversion and a faster interfacial charge transfer rate is observed after ALD Al₂O₃ overcoating (Figure S13).

It is a great challenge to maintain the size and morphology of Cu-based nanoparticle catalysts during CO₂RR and achieve long-term stability for producing specific C₂₊ products. Both the total current density (*j*_{total}) and FE_{C₂H₄} gradually decrease for Cu NCs held at –1.1 V vs. RHE, while negligible performance degradation is observed for Cu NCs/Al₂O₃-10C (Figure S14). The initially monodisperse Cu NCs aggregated into larger clusters with a wider size distribution range after 12 h electrolysis at –1.1 V vs. RHE (Figure S15a and b). The severe aggregation of Cu NCs leads to a 45.8% decrease of ECSA and 79.5% decrease in the ratio of (100)/(111) on nanocrystal surfaces (Figure S16). However, there is only a slight decrease, from 7.45 to 6.84, in (100)/(111) over the Cu NCs/Al₂O₃-10C after electrolysis. By contrast, these critical properties for Cu NCs/Al₂O₃-10C are well maintained since the Al₂O₃ overcoating physically separates the nanocrystals and reduces the chance of migration and collision during CO₂RR (Figure S15c and d). A slight surface reduction is observed on Cu NC/Al₂O₃-10C after electrolysis, suggesting that the metallic Cu⁰ species act as the active sites for selective CO₂RR (Figure S17).^[29] In situ small angle X-ray scattering (SAXS) measurements using a custom-made electrochemical flow cell were carried out to track the size evolution of Cu NCs-based catalysts during CO₂RR (Figure 3d and Figure S18). After 1 h electrolysis at –1.1 V vs. RHE, the mean size diameter for Cu NCs increases from 10.1 nm to 14.8 nm and relative number density decreases to 59.6% after 1 h electrolysis at –1.1 V vs. RHE (Figure 3e), suggesting that NC aggregation is likely the dominant mechanism for CO₂RR activity degradation. By contrast, the ultrathin Al₂O₃ overcoating mitigates the severe NC aggregation resulting in smaller changes of mean size diameter and relative number density.

In order to remove CO₂ mass transfer limitations and achieve higher partial current density towards ethylene production, we utilized a gas-feed flow electrolyzer to test the CO₂RR activity of Cu NCs/Al₂O₃-10C in 5 M KOH electrolyte (Figure 4a and Figure S19). A PTFE-based gas diffusion electrode (GDE) with high surface hydrophobicity

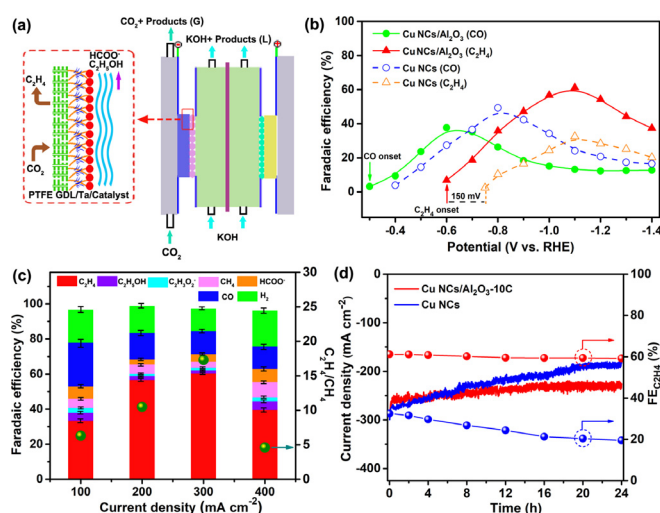


Figure 4. a) Schematic diagram of the gas-feed flow electrolyzer with PTFE-based GDE configuration. b) A comparison of the potential-dependent FE_{CO} and FE_{C₂H₄} for Cu NCs and Cu NCs/Al₂O₃-10C in 5 M KOH electrolyte. c) FE of product distribution for Cu NCs/Al₂O₃-10C as a function of current density. The resistance of the three-electrode system under OCV was evaluated and then 90% value for IR compensation was applied. d) Stability test of Cu NCs and Cu NCs/Al₂O₃-10C conducted at –1.1 V vs. RHE for 24 h.

was used as the substrate to avoid the typical “flooding” issue that is common for carbon-based GDEs.^[30] Inert tantalum was sputtered onto the PTFE to endow the electrode with high conductivity without affecting the CO₂RR of tested catalysts (Figure S20). The increase of KOH concentration provides higher electrolyte conductivity and lower ohmic losses which facilitates a larger current density (Figure S21). pH increase also suppresses the competing hydrogen evolution reaction (HER), together with the positive effect of the triple-boundary interface in promoting C–C coupling, as supported by the DFT calculations and other reported research.^[31] A 150 mV shift in onset potential from Cu NCs to Cu NCs/Al₂O₃-10C is observed experimentally (Figure 4b). These observations can be explained by the DFT calculations showing a 0.11 eV decrease of the reaction energy barrier of the C–C coupling step after ALD overcoating. CO is the dominant product below –0.6 V vs. RHE, with FE_{CO} being as high as 40% at –0.6 V vs. RHE. As the potential becomes more negative, FE_{CO} decreases while FE_{C₂H₄} increases, suggesting that *CO intermediates play a critical role in the C–C coupling step to form C₂H₄.^[28] Cu NCs/Al₂O₃-10C shows a considerably higher peak FE_{C₂H₄} of 61.2% at –1.1 V vs. RHE, when compared with the Cu NCs (FE_{C₂H₄} = 32.5%). As shown in Figure 4c, Cu NCs/Al₂O₃-10C achieves a FE_{C₂H₄} of 60.4% at a high current density of 300 mA cm⁻², corresponding to a partial current density towards C₂H₄ (*j*_{C₂H₄}) as high as 181.2 mA cm⁻². The corresponding FE_{C₂H₄}/FE_{CH₄} ratio reaches a maximum of 17.3, indicating that the reaction pathway of CO₂-to-C₂H₄ conversion is more favorable, and CH₄ generation is significantly suppressed in the basic solution.^[32] The remarkable FE_{C₂H₄} and *j*_{C₂H₄} make Cu NCs/Al₂O₃-10C superior to the reported colloidal Cu NCs-based electrocatalysts in the gas-feed flow

electrolyzer with strong alkaline electrolyte, such as Cu nanocubes^[7] ($\text{FE}_{\text{C}_2\text{H}_4} = 60\%$, $j_{\text{C}_2\text{H}_4} = 144 \text{ mA cm}^{-2}$) and Cu cubes^[33] ($\text{FE}_{\text{C}_2\text{H}_4} = 57\%$, $j_{\text{C}_2\text{H}_4} = 171 \text{ mA cm}^{-2}$). Stability tests for CO_2 electrolysis were carried out at a constant potential of -1.1 V vs. RHE in 5 M KOH . The j_{total} and $\text{FE}_{\text{C}_2\text{H}_4}$ displayed a smaller drop of 9.7% and 3.3% within 24 h electrolysis on Cu NCs/ Al_2O_3 -10C at -1.1 V vs. RHE, compared to 39.0% and 40.0% decay for Cu NCs, respectively (Figure 4d). A continuous size evolution from monodisperse nanoparticles to large aggregated clusters was observed on Cu NCs over time, whereas ALD overcoating effectively minimized the motion of Cu NCs driven by the electric field or adsorption/desorption of intermediates under the harsh conditions of high current density and pH (Figure S22).^[34]

Conclusion

In summary, we used ALD to deposit ultrathin Al_2O_3 onto supported Cu NCs to selectively cover (111) facets by switching the precursor pulse sequences. The overcoated Cu NCs with a high ratio of (100)/(111) not only display remarkable improvement of C_2H_4 faradaic efficiency and suppression of CH_4 generation, but also prevent the dynamic motion and aggregation of the NCs under harsh conditions. In a gas-feed flow electrolyzer in 5 M KOH , Cu NCs/ Al_2O_3 -10C achieves a high $\text{FE}_{\text{C}_2\text{H}_4}$ of 60.4% with a current density of -300 mA cm^{-2} and negligible activity/selectivity degradation over 24 h . This facet-selective deposition strategy shows promise as a general approach for tuning the selectivity and enhancing the stability of CO_2 RR on Cu NCs-based catalysts.

Acknowledgements

The material for the synthesis of Cu nanocrystals, ALD overcoating, and all electrochemical measurements is primarily supported by the Joint Center for Artificial Photosynthesis, a DOE Energy Innovation Hub, supported through the Office of Science of the U.S. Department of Energy, under Award No. DE-SC0004993. P.P.Y. and T.C. thank the National Natural Science Foundation of China (21903058), the Natural Science Foundation of Jiangsu Higher Education Institutions (SBK20190810) for financial support. R.L. and X.W. acknowledge the support from NSFC (51961165105) and Guangdong Basic and Applied Basic Research Foundation (2020B1515120039). This research used beamline 7.3.1 of the Advanced Light Source, a U.S. DOE Office of Science User Facility under contract no. DE-AC02-05CH11231, and beamline 1–5 of the Stanford Synchrotron Radiation Light-source, SLAC National Accelerator Laboratory, supported by the U.S. Department of Energy, Office of Science, Office of Basic Energy Sciences under contract no. DE-AC02-76SF00515.

Conflict of Interest

The authors declare no conflict of interest.

Keywords: atomic layer deposition · CO_2 reduction · copper nanocrystals · facet-selective · stability

- [1] S. Nitopi, E. Bertheussen, S. B. Scott, X. Liu, A. K. Engstfeld, S. Horch, B. Seger, I. E. L. Stephens, K. Chan, C. Hahn, J. K. Nørskov, T. F. Jaramillo, I. Chorkendorff, *Chem. Rev.* **2019**, *119*, 7610–7672.
- [2] J. Huang, R. Buonsanti, *Chem. Mater.* **2019**, *31*, 13–25.
- [3] V. Mantella, L. Castilla-Amoros, R. Buonsanti, *Chem. Sci.* **2020**, *11*, 11394–11403.
- [4] Y. Hori, I. Takahashi, O. Koga, N. Hoshi, *J. Phys. Chem. B* **2002**, *106*, 15–17.
- [5] I. Takahashi, O. Koga, N. Hoshi, Y. Hori, *J. Electroanal. Chem.* **2002**, *533*, 135–143.
- [6] A. Loiudice, P. Lobaccaro, E. A. Kamali, T. Thao, B. H. Huang, J. W. Ager, R. Buonsanti, *Angew. Chem. Int. Ed.* **2016**, *55*, 5789–5792; *Angew. Chem.* **2016**, *128*, 5883–5886.
- [7] Y. Wang, H. Shen, K. J. T. Livy, D. Raciti, H. Zong, J. Gregg, M. Onadeko, Y. Wan, A. Watson, C. Wang, *Nano Lett.* **2019**, *19*, 8461–8468.
- [8] J. Huang, N. Hormann, E. Oveisi, A. Loiudice, G. L. D. Gregorio, O. Andreussi, N. Marzari, R. Buonsanti, *Nat. Commun.* **2018**, *9*, 3117.
- [9] P. Wilde, P. B. O'Mara, J. R. C. Junqueira, T. Tarnev, T. M. Benedetti, C. Andronescu, Y. T. Chen, R. D. Tilley, W. Schuhmann, J. J. Gooding, *Chem. Sci.* **2021**, *12*, 4028–4033.
- [10] S. Popović, M. Smiljanić, P. Jovanović, J. Vavra, R. Buonsanti, N. Hodnik, *Angew. Chem. Int. Ed.* **2020**, *59*, 14736–14746; *Angew. Chem.* **2020**, *132*, 14844–14854.
- [11] Y. T. Guntern, J. R. Pankhurst, J. Vavra, M. Mensi, V. Mantella, P. Schouwink, R. Buonsanti, *Angew. Chem. Int. Ed.* **2019**, *58*, 12632–12639; *Angew. Chem.* **2019**, *131*, 12762–12769.
- [12] Z. Cao, D. Kim, D. Hong, Y. Yu, S. Lin, X. Wen, E. M. Nichols, K. Jeong, J. A. Reimer, P. Yang, C. J. Chang, *J. Am. Chem. Soc.* **2016**, *138*, 8120–8125.
- [13] K. Cao, J. Cai, B. Shan, R. Chen, *Sci. Bull.* **2020**, *65*, 678–688.
- [14] E. Sarnello, Z. Li, S. Seifert, R. E. Winans, T. Li, *ACS Catal.* **2021**, *11*, 2605–2619.
- [15] J. Lu, B. Fu, M. C. Kung, G. Xiao, J. W. Elam, H. H. Kung, P. C. Stair, *Science* **2012**, *335*, 1205–1208.
- [16] Z. Lu, R. W. Tracy, M. Leigh Abrams, N. L. Nicholls, P. T. Barger, T. Li, P. C. Stair, A. A. Dameron, C. P. Nicholas, C. L. Marshall, *ACS Catal.* **2020**, *10*, 13957–13967.
- [17] N. Cheng, M. N. Banis, J. Liu, A. Riese, X. Li, R. Li, S. Ye, S. Knights, X. Sun, *Adv. Mater.* **2015**, *27*, 277–281.
- [18] K. Cao, J. Cai, X. Liu, R. Chen, *J. Vac. Sci. Technol. A* **2018**, *36*, 010801.
- [19] K. Cao, L. Shi, M. Gong, J. Cai, X. Liu, S. Chu, Y. Lang, B. Shan, R. Chen, *Small* **2017**, *13*, 1700648.
- [20] Y. Wen, J. Cai, J. Zhang, J. Yang, L. Shi, K. Cao, R. Chen, B. Shan, *Chem. Mater.* **2019**, *31*, 101–111.
- [21] J. Lu, B. Liu, N. P. Guisinger, P. C. Stair, J. P. Greeley, J. W. Elam, *Chem. Mater.* **2014**, *26*, 6752–6761.
- [22] D. Kim, C. S. Kley, Y. Li, P. Yang, *Proc. Natl. Acad. Sci. USA* **2017**, *114*, 10560–10565.
- [23] E. Levrau, K. V. Kerckhove, K. Devloo-Casier, S. P. Sree, J. A. Martens, C. Detavernier, J. Dendooven, *J. Phys. Chem. C* **2014**, *118*, 29854–29859.
- [24] S. Nikafshar, O. Zabihi, Y. Moradi, M. Ahmadi, S. Amiri, M. Naebe, *Polymers* **2017**, *9*, 266.
- [25] R. Zhao, Y. Gao, Z. Guo, Y. Su, X. Wang, *ACS Appl. Mater. Interfaces* **2017**, *9*, 1885–1890.
- [26] H. S. Jeon, J. Timoshenko, F. Scholten, I. Sinev, A. Herzog, F. T. Haase, B. R. Cuenya, *J. Am. Chem. Soc.* **2019**, *141*, 19879–19887.
- [27] A. Gharachorlou, M. D. Detwiler, X. K. Gu, L. Mayr, B. Klotzer, J. Greeley, R. G. Reifengerger, W. N. Delgass, F. H. Ribeiro,

- D. Y. Zemlyanov, *ACS Appl. Mater. Interfaces* **2015**, *7*, 16428–16439.
- [28] J. H. Monotoya, C. Shi, K. Chan, J. K. Norskov, *J. Phys. Chem. C* **2015**, *119*, 2032–2037.
- [29] S. B. Scott, T. V. Hogg, A. T. Landers, T. Maagaard, E. Bertheussen, J. C. Lin, R. C. Davis, J. W. Beeman, D. Higgins, W. S. Drisdell, C. Hahn, A. Mehta, B. Seger, T. F. Jaramillo, I. Chorkendorff, *ACS Energy Lett.* **2019**, *4*, 803–804.
- [30] M. E. Leonard, L. E. Clarke, A. Forner-Cuenca, S. M. Brown, F. R. Brushett, *ChemSusChem* **2020**, *13*, 400–411.
- [31] C. T. Dinh, T. Burdyny, M. G. Kibria, A. Seifitokaldani, C. M. Gabardo, F. P. G. Arquer, A. Kiani, J. P. Edwards, P. D. Luna, O. S. Bushuyev, C. Zou, R. Quintero-Bermudez, Y. Pang, D. Sinton, E. H. Sargent, *Science* **2018**, *360*, 783–787.
- [32] S. E. Weitzner, S. A. Akhade, J. B. Varley, B. C. Wood, M. Otani, S. E. Baker, E. B. Duoss, *J. Phys. Chem. Lett.* **2020**, *11*, 4113–4118.
- [33] G. L. De Gregorio, T. Burdyny, A. Loiudice, P. Iyengar, W. A. Smith, R. Buonsanti, *ACS Catal.* **2020**, *10*, 4854–4862.
- [34] W. T. Osowiecki, J. J. Nussbaum, G. A. Kamat, G. Katsoukis, M. Ledendecker, H. Frei, A. T. Bell, A. P. Alivisatos, *ACS Appl. Mater. Interfaces* **2019**, *11*, 7744–7749.
- Manuscript received: July 18, 2021
Revised manuscript received: August 24, 2021
Accepted manuscript online: September 20, 2021
Version of record online: October 13, 2021
-